

Hyperspectral Brain Imaging

Project 4087

Department of Bioengineering
Imperial College London

*A Project Report Submitted in
Partial Fulfilment of the*

MEng Biomedical Engineering / Molecular Bioengineering Degree

Supervisors:

Dr Amanda Foust
a.foust@imperial.ac.uk

Dr Akhil Kallepalli
a.kallepalli@imperial.ac.uk

Prof Simon Schultz
s.schultz@imperial.ac.uk

Department of Bioengineering

April, 2024

Project 4087: Hyperspectral Brain Imaging

Aveek Goswami, Cameron Rahul Sah Briginshaw, Hafsa Waseem,
Rachael Soh Hui Kie, Tze Kye Amos Koh, Wei Han Low

April 15, 2024

Abstract

Push-broom hyperspectral imaging is a technique used to collect full spectral and spatial information of a target line by line. This imaging method that reconstructs images as a function of wavelength has proven to be useful in industrial, airborne, and satellite applications such as target recognition and classification. More recently, a foray into applying this technique to applications like diagnosis and health monitoring has displayed huge potential in revealing insights into medical conditions and treatments. However, the hyperspectral imagers used for these studies have been costly and inaccessible. Hence, this project aims to investigate the feasibility of applying a low-cost hyperspectral imager to microscopic medical applications.

This paper details the materials and methods used to construct, calibrate, and test a low-cost hyperspectral camera. The push-broom hyperspectral imaging system was validated by comparing the data obtained from imaging ischaemic and non-ischaemic human fingers. Results show that images of the target objects could be reconstructed, albeit with insufficient resolution to accurately differentiate the fingers. Due to the limited useable finger images obtained using the camera, images from an open-source database were used to evaluate the efficacy of different methods used to perform pre-processing and endmember analysis. It was concluded that these methods were successful proofs of concepts that the device and aspects of processing strategies worked. This serves as a starting point to further investigate how the hyperspectral camera can be integrated into a common laboratory microscope for micro-scale medical imaging.

1 Introduction

1.1 Background on Hyperspectral Imaging (HSI)

Hyperspectral imaging (HSI) is a technique used to capture images with high spectral resolution. General-purpose cameras have three spectral bands corresponding to red (R), green (G) and blue (B) wavelengths of light, and multispectral cameras involve several discrete spectral bands. However, images captured by these cameras lack the spectral resolution required to detect subtle compositional differences in target objects. Comparatively, as shown in Figure 1, HSI col-

lects a target's spectral data across a large number (hundreds) of wavelengths, forming what is effectively a continuous spectrum. This is done for each pixel of data in an image using a push-broom mechanism, which images slices of a target in a fixed direction (Sigernes et al., 2018). The resulting spectrogram corresponds to the entrance slit image at that point along a track, as demonstrated in Figure 2. Then, the intensity values at each wavelength of the spectrogram are added as a third dimension to the two-dimensional (2D) spatial image. Spectrograms can be stacked at a high speed to form a hypercube containing two spatial dimensions and one spectral dimension (Yuen and Richardson, 2010). HSI therefore provides more spectral information for detailed analysis and classification

tasks (Feng et al., 2020), surpassing the limitations of traditional RGB and multispectral imaging.

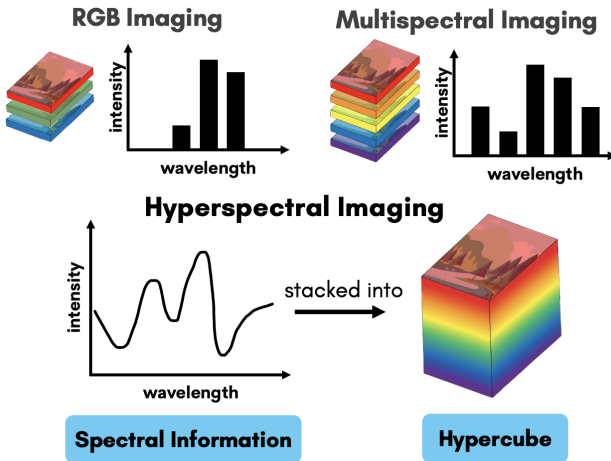


Figure 1: RGB vs Multispectral vs HSI, adapted from Edmund Optics (2024)

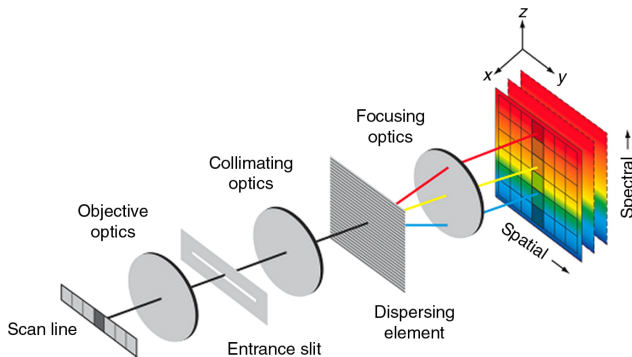


Figure 2: HSI Overview, adapted from Dell'Endice et al. (2009)

1.2 Existing Literature

Existing HSI applications primarily focus on macroscopic uses such as remote sensing for environmental monitoring (van der Meer et al., 2012), agricultural assessment (Caballero et al., 2020), military surveillance (Shimoni et al., 2019), and food inspection (Feng and Sun, 2012).

However, advances in hyperspectral cameras, image analysis methods, and computational power are making it increasingly possible for many exciting applications at the microscopic level in the medical field. This is because the hyperspectral image of reflected light includes rich information about the structural and biochemical features of human tissue. According to Yoon (2022), light delivered to biological tissue undergoes multiple scattering (due to inhomogeneity of biological structures) and absorption as it propagates through the

tissue. It is assumed that the absorption, fluorescence, and scattering characteristics of tissue change during the progression of disease. Therefore, the reflected, fluorescent, and transmitted light from tissue captured by HSI carries quantitative diagnostic information about tissue pathology. Hence, the nature of HSI offers great potential for non-invasive disease diagnosis and surgical guidance. For example, the retina can be externally imaged using HSI techniques to identify accumulation of Alzheimer's pathology, usually only found within brain tissue (Hadoux et al., 2019).

According to Lu and Fei (2014), current medical HSI systems can prove costly and impractical for extensive use. Nonetheless, advances in technology have also led to the development of affordable and easily assembled HSI systems. Sigernes et al. (2018) first devised the concept of a do-it-yourself hyperspectral imager that can be built using readily available off-the-shelf parts. The study successfully showed that these instruments were capable of pushbroom hyperspectral imaging from various platforms, across both airborne drone and handheld operations. This study motivated future work in this field such as the building of a plug-and-play hyperspectral imager by Salazar-Vazquez and Mendez-Vazquez (2020) whose work introduced methods to further decrease the complexity and processing time required in obtaining high-resolution spectra. However, all previous studies on low-cost HSI systems focused on applying their systems on macroscopic applications. Thus, this project aims to explore the potential of applying low-cost HSI systems on the microscopic level, evaluating its ability to obtain insights about medical phenomena.

1.3 Project Overview and Objective

This project builds on the existing studies mentioned above by adapting a low-cost HSI system to be applied on a microscopic scale and in a medical context. The aim was to build a HSI system that can be easily assembled using off-the-shelf parts that are readily available and inexpensive, and explore how this system can enhance the capabilities of a microscope for brain tissue imaging and analysis. A combination of 3D Computer Aided Design (CAD) and optical components were used to construct the HSI camera. Spectrograms captured by the camera were reconstructed into data hypercubes, which were then analysed through various methods. Our system was first tested with a finger ischaemia experiment to evaluate its functionality. Image processing algorithms were then developed to isolate the constituent spectra corresponding to different features in brain tissue. Subsequently, the system can be further validated by testing its capability to obtain spectrograms of mouse brain tissue with Alzheimer's Disease, with the goal to gain more insights into the lo-

cation and abundance of specific biomarkers that would not have been possible to obtain through imaging via a regular light microscope.

Ultimately, this project investigates a novel application of low-cost HSI, and a successful implementation of the system sets a precedent for the widespread use of HSI for disease pathology analysis across a range of medical fields.

2 Methods

2.1 Building the HSI System

The HSI system was built mainly referencing the imager devised by Sigernes et al. (2018).

2.1.1 Optics Theory

Figure 3 depicts an optics schematic of the HSI device. Light reflected off the object being imaged is incident on the front lens, which focuses the light before it passes through the precision air slit. The slit allows a $20\mu\text{m}$ wide slice of light, corresponding to a specific location on the object, to pass through. The field lens redirects diverging light beams from the slit (Riedl, 2001) towards the collimator lens, which transforms the light into a parallel beam that hits the transmission grating (Morris, 2021).

The transmission grating splits the light into its component wavelengths through a series of closely spaced grooves. When light hits the grooves, it spreads out due to diffraction, creating a spectrum (Wang et al., 2022). Finally, the detector lens focuses the diffracted light onto the detector array. The detector captures the spectral data, which can be displayed as a spectral image, as shown in Figure 4.

2.1.2 Parts Used

Figure 5 shows an exploded view of our system excluding the detector, which comes after Part 9. The parts are labelled as shown in Table 1, and the cost per part are shown in the Bill of Materials in Section 6.1.

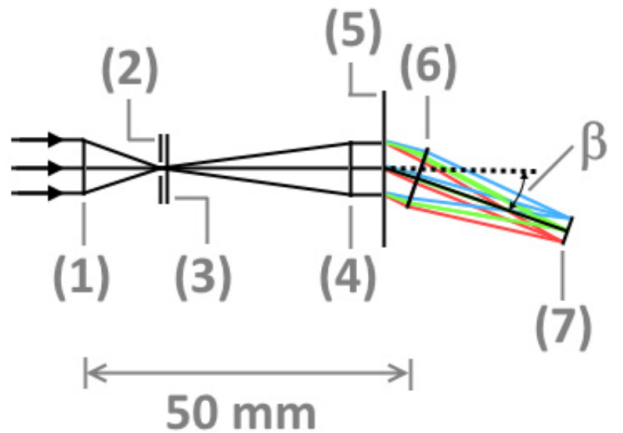


Figure 3: HSI Optics Schematic: (1) Front lens, (2) Entrance slit, (3) Field lens, (4) Collimator lens, (5) Transmission grating, (6) Detector lens. Adapted from Sigernes et al. (2018)

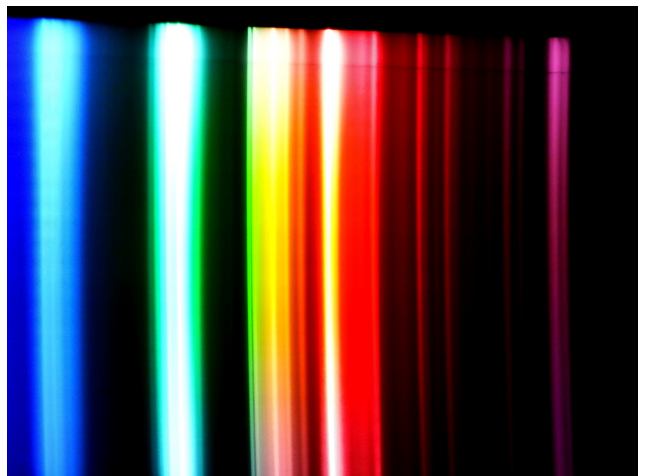


Figure 4: White Light Spectrogram

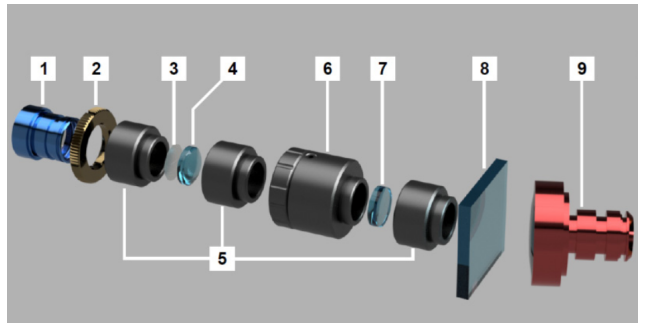


Figure 5: HSI Camera Exploded View, from Sigernes et al. (2018)

Part #	Description
1	Front lens
2	M12 lock nut
3	Precision air slit
4	Field lens
5	Lens mounts
6	S-mount focus tube
7	Collimator lens
8	Transmission grating
9	Detector lens

Table 1: Part Description

The Spinel 8MP camera - Figure 6, was selected for its affordable price and USB connectivity. CMOS cameras are preferable for HSI, as RGB cameras contain extra filters that change the raw data collected. However, most CMOS cameras are costly. The Spinel 8MP camera has a CMOS sensor, but streams videos in the YUV data format. The Y channel corresponds to luminance and records the monochrome data from the scene. The camera's native software, AMCap, was used to vary imaging parameters.

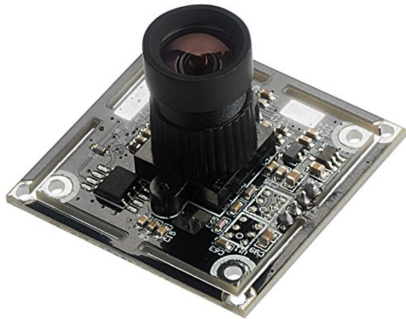


Figure 6: Spinel 8MP Detector with Sony IMX179 sensor

Materials were sourced from Edmund Optics and Thorlabs, and the total cost of the final system design was £634.62. This is extremely low-cost, considering that existing hyperspectral cameras cost upward of £30,000 (e.g. Specim FX17e), with commercial systems costing far more (Stuart et al., 2020).

2.1.3 3D-Printed Housing

The optics assembly was housed in a 3D-printed case, pictured in Figure 7. The housing held the system in place and aligned the optics for accurate light dispersion. Additionally, it protected the delicate parts from oils and dust to minimize artefacts on the spectrograms. Crucially, the housing prevented ambient white

light from interfering with the spectra of the target object. A CAD file created by The OpenHSI Project (Mao et al., 2022) was modified using Solidworks and 3D-printed using PLA.



Figure 7: 3D Printed HSI Camera Housing

2.1.4 System Assembly

The system was assembled within the housing as shown in Figure 8. Each lens was adjusted to sit flat within the lens mounts and the slit was centralised and oriented vertically to the surface. The camera was attached to the detector lens, and its orientation was adjusted such that the spectrum obtained was horizontal.



Figure 8: Final HSI Camera Assembly

2.2 Acquiring a Spectrogram

A spectrogram depicts the intensity of different wavelengths of light for a target region. Using the assembly described in Figure 3, a slice of an object is imaged, providing the spectrogram of a column of pixels. The intensity across the slice's width was averaged to produce a 2D spectrogram representing the intensity of

that column across different wavelengths. The spatial dimension y represents the column height, and a spectral dimension z represents the different spectrum wavelengths. These 2D spectrograms can be stacked along their widths (x-axis) to form a hypercube, as represented in Figure 9.

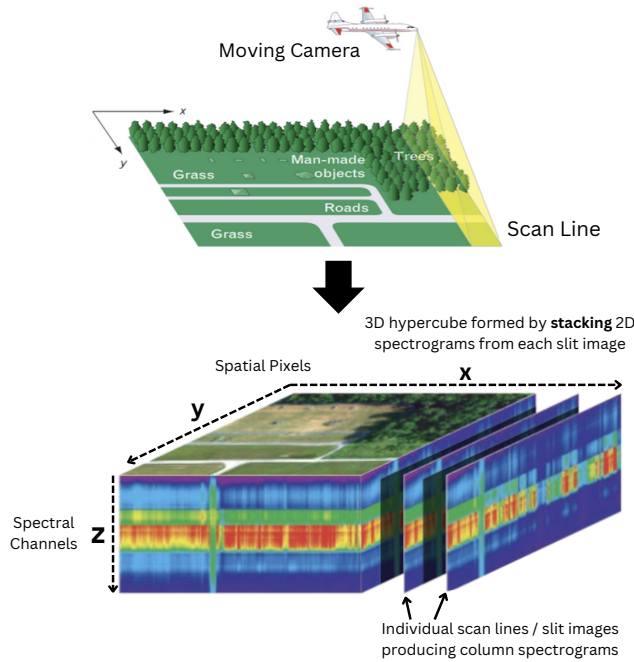


Figure 9: Stacking of slit images to form hypercube
adapted from Shaw and Burke (2003)

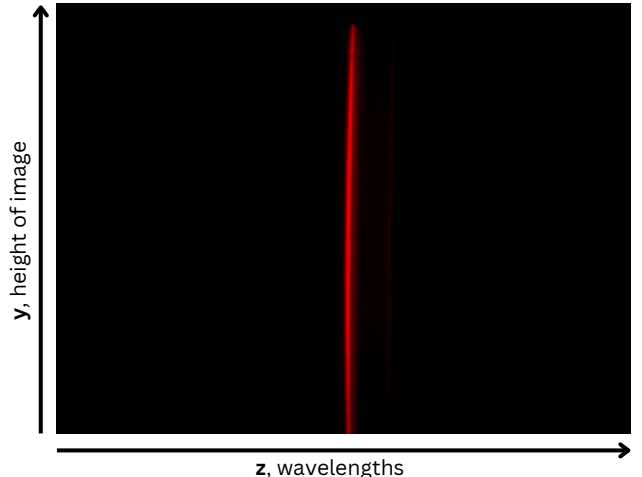


Figure 10: Column spectra for red light

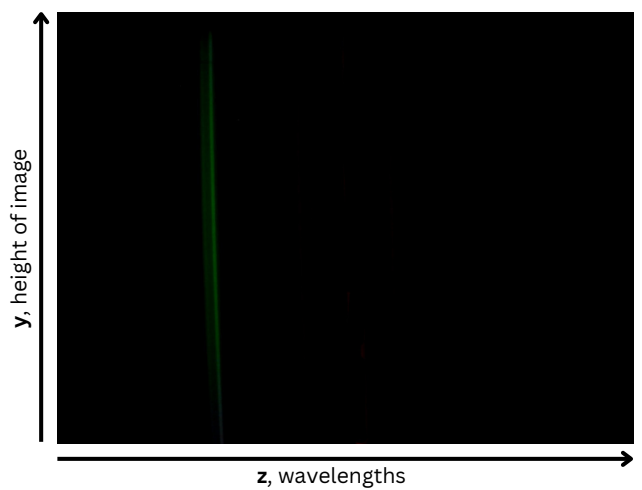


Figure 11: Column spectra for green light

2.2.2 Calculating the Field of View

The Field of View (FOV) of the camera must contain the object of interest, which was ensured by manipulating the distance between the camera and the object. For the finger ischaemia test as described in Section 2.3, the process for determining the appropriate distance is illustrated in Figure 12.

The distance to place the finger from the object, **D1**, needed to be calculated to ensure that the entire finger width was within the FOV as depicted in Figure 12b. **D1**, **D2**, slit height **H** and finger width **FW** are related by the magnification, **M**, of the front lens as shown in Equation 1 (Hollows and James, 2024).

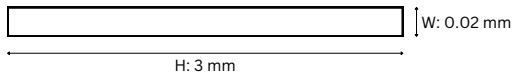
$$M = \frac{H}{FW} = \frac{D2}{D1} \quad (1)$$

The values **H**, **FW** and **D2** are fixed, and the minimum

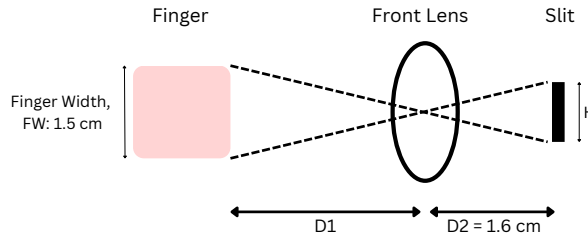
2.2.1 Calibrating the Spectrogram

The spectrogram required calibration so that bands of intensity could be accurately assigned to their wavelengths. White light was reflected off red, green and blue true-colour images towards the camera. This produced a column spectra with a visible line as shown in Figures 10 and 11. The z -coordinate of the line was taken to correspond to the wavelength of the colour that produced that reflected light. Repeating this process produced three z -coordinates for three wavelengths, which were then extrapolated to obtain the wavelengths for the rest of the visible light spectrum (Heo, 2019).

(a) Slit Dimensions (displayed after rotating)



(b) To capture entire width of finger in FOV



(c) Capturing incremental sections, c, of the finger's length

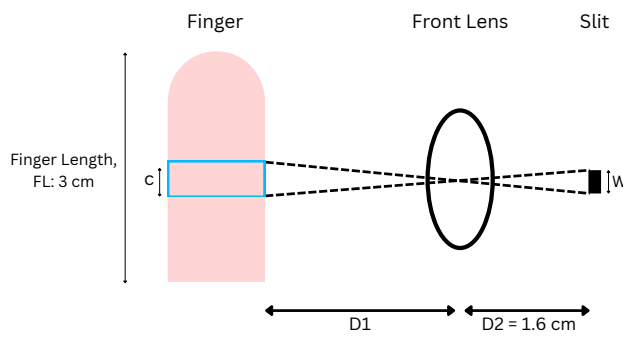


Figure 12: FOV calculations for finger (not to scale)

value of **D1** was calculated:

$$D1 = \frac{FW}{H} \times D2 = \frac{1.5 \times 10^{-2}}{3 \times 10^{-3}} \times 1.6 \times 10^{-2} \\ = 0.08 \text{ m} \\ = 8 \text{ cm}$$

Giving the finger a tolerance of 0.25cm on either side, the value of **D1** calculated and used was 10.8cm as shown:

$$D1 = \frac{FW}{H} \times D2 = \frac{(1.5 + 2(0.25)) \times 10^{-2}}{3 \times 10^{-3}} \times 1.6 \times 10^{-2} \\ = 0.108 \text{ m} \\ = 10.8 \text{ cm}$$

Next, given **D1** and **D2**, the length of the finger captured in the FOV can be calculated using the same equation, but using the slit width as shown in Figure 12c. This value **C** corresponds to the column of pixels obtained from a single slit image. This calculation further indicates that to be entirely captured without overlaps or gaps between images, the finger needs to

move by increments of **C**. The value of **C** can hence be calculated to be 0.0135cm as shown:

$$M = \frac{W}{C} = \frac{D2}{D1} \\ C = \frac{D1}{D2} \times W = \frac{10.8}{1.6} \times 0.02 \times 10^{-3} \\ = 0.135 \times 10^{-3} \text{ m} \\ = 0.0135 \text{ cm}$$

2.3 The Finger Ischaemia Test Proof of Concept

Ischemia is a condition in which blood flow is restricted in a part of the body. As this causes changes in reflectance properties (De Winne et al., 2024), HSI can detect regions and levels of ischemia in a non-invasive manner, as shown by Akbari et al. (2008). Therefore, the finger ischemia test was used to confirm the functionality of the HSI system.

Key Steps:

1. Record spectrogram across an image target using video capture
2. Construct hypercube datasets for ischaemic and non-ischaemic finger
3. Analyse hypercube datasets in MATLAB
4. Reconstruct images of fingers

2.3.1 Experiment Set-Up

The pushbroom method involves recording a spectrogram along a single spatial line at each moment in time. The target is moved across a plane to capture the spectra of the entire target.

The experimental set-up is shown in Figure 13. The camera is suspended above the finger, which moves at a constant speed as the camera captures a live video feed. Each frame in the video represents a spectrogram derived from a single scan line.

From Section 2.2, the camera was positioned 10.8cm away from the finger and each slit image captures 0.0135cm of the finger's length. For a 4cm long target region, $\frac{4}{0.0135} = 300$ incremental images were required, which would be stacked to fully construct the hypercube of the finger. Markings were made on the table to assist our subject in moving their finger. The subject then moved their finger such that the camera recorded



Figure 13: Set-up for finger ischaemia imaging

the entire length of the finger in 150 seconds at 2 frames per second, producing $150 \times 2 = 300$ frames.

2.3.2 Construction of the Hypercube Dataset

A MATLAB routine was written to process the video captured by the HSI system.

Methodology:

- Frame Extraction:** The 150-second video was sampled at regular intervals to obtain 900 frame samples, where $t_{interval} = \frac{\text{video duration}}{\text{number of frames}}$.
- Frame processing:** frame arrays were resized by $0.25 \times$ and converted from RGB to Y (luminance) representation. They were then normalized to a $[0,1]$ scale by dividing by 255.
- Hypercube construction:** As the script iterates through the frames, it processes and stores the Y component of each frame to form the hypercube.

Sampling 900 frames from the video, where some frames are repeated, improved the spatial resolution of the hypercube for better image reconstruction in subsequent sections. The conversion from RGB to Y isolates the monochromatic intensity information.

The constructed hypercube matrix has dimensions $n \times x \times s$, where n is the FOV height, m is the length of the target scanned, and s is the length of the spectrogram. The n -th frame of the video is stored in the n -th column of the hypercube.

2.3.3 Reconstruction of the Image from the Hypercube

MATLAB has an inbuilt Hyperspectral Image Processing toolbox to reconstruct images from a hypercube object. The composite image provides an intuitive overview of the system's overall imaging capabilities, mainly how well it resolves spectral and spatial data.

A MATLAB hypercube object was initialised with the hypercube dataset and calibrated with wavelength data. The `colorize` function was then used to interpret the spectral data within the hypercube, translating the spectral information across space back into a composite image that can be displayed.

2.4 Hyperspectral Preprocessing & Analysis

The constructed hypercubes had low resolution and precision due to the innate technical limitations of the camera, thus image processing and analysis on the collected images could be potentially futile. Hence, proof of concept algorithms were developed for an image (shown in Figure 14) sourced from an existing medical HSI database compiled by Fabelo et al. (2019). An image processing pipeline was created for application on the low-cost HSI system to improve the signal to noise ratio (SNR) and identify medically important features.



Figure 14: Image of brain tissue from Fabelo et al. (2019)

2.4.1 Preprocessing

The preprocessing pipeline was largely derived from the scheme used by Callico et al. (2018). Major steps were – radiometric calibration, noise filtering, band reduction and normalization. Parallel computing in MATLAB was used to handle the large dimensionality of hyperspectral data.

Radiometric Calibration

The calibration was done using equation 2 (Shaikh et al., 2021).

$$\text{reflectance} = 100 \times \frac{m - d}{w - d}. \quad (2)$$

m : original reflectance measurement

d : dark reference

w : white reference

Corruption Removal

Many images in the hyperspectral dataset had varying degrees of corruption as shown in Figure 15. This corruption was manually cropped out.



Figure 15: Corruption Within Dataset Image

Noise Filtering

A multiple regression based approach was used, assuming that reflectance values are predictable based on the values at other wavelengths. The residuals of this regression were taken as an estimate of the noise, and a version of the HySIME algorithm (Nascimento and Bioucas-Dias, 2007) was applied. HySIME was then used to find the signal subspace that contained the useful signal. The noise filtering algorithm used was adapted from the psyptools python library (Therien, 2018).

For spectral data, represented by a matrix Y of dimensions $L \times N$, the covariance matrix RR is computed:

$$RR_{ij} = \frac{1}{N} \sum_{k=1}^N Y_{ik} Y_{jk} \quad \forall i, j = 1, \dots, L$$

L : number of spectral bands

N : number of pixels

Regularization is applied to ensure RR is positive definite:

$$RR = RR + \epsilon I$$

where ϵ is a small constant. The inverse of RR is then computed for regression:

$$RR_{\text{regularized}}^{-1} = \text{pinv}(RR)$$

Noise for each band is estimated by regression against all other bands:

$$\hat{\beta}_i = RR_{-i}^{-1} Y_{-i}, \quad \hat{w}_i = Y_i - \hat{\beta}_i^\top Y$$

The additive noise model assumes r is a spectral band and Z includes all other bands. The noise model is defined by:

$$r = Z\beta + \xi, \quad \hat{\beta} = (Z^\top Z)^{-1} Z^\top r, \quad \hat{\xi} = r - Z\hat{\beta}$$

The noise covariance matrix R_n is estimated:

$$R_n = \text{diag} \left(\frac{1}{N} \sum_{k=1}^N \hat{\xi}_{ik}^2 \right)$$

Estimating the signal subspace given the noise-subtracted data matrix X :

$$R_x = \frac{1}{N} (X - N)(X - N)^\top$$

Eigendecomposition of R_x :

$$R_x = E D E^\top$$

The dimension k_f of the signal subspace is selected based on the eigenvectors corresponding to the largest eigenvalues:

$$k_f = \arg \min_k (\text{tr}((I - U_k) R_y) + 2\text{tr}(U_k R_n))$$

where U_k is the projection matrix onto the subspace spanned by the first k eigenvectors.

Once identified, the hyperspectral data is projected onto this signal subspace to filter out noise:

$$\text{DenoisedHSI2D} = E_k (E_k^\top \text{HSI2D})$$

where E_k consists of the first k_f columns of E , which contain the eigenvectors associated with the largest eigenvalues determined by the HySIME method. HSI2D represents the reshaped hyperspectral data into a 2D matrix where each column is a pixel's spectrum.

Band Reduction

Due to information redundancy between contiguous bands, the spectral signatures are reduced via spectral averaging to produce 129 bands.

Normalization

Building upon research from Cao et al. (2017), a “global max-min” normalisation method is used, standardising the range of wavelength intensities across the dataset from 0 to 1.

1. Flatten the hypercube into a single vector:

$$\text{vec}(\mathbf{H}) = \begin{bmatrix} \mathbf{H}_{1,1,1} \\ \mathbf{H}_{1,1,2} \\ \vdots \\ \mathbf{H}_{H,W,B} \end{bmatrix}$$

2. Compute the global minimum and maximum values across the entire dataset:

$$\text{minVal} = \min(\text{vec}(\mathbf{H})), \quad \text{maxVal} = \max(\text{vec}(\mathbf{H}))$$

3. Apply the normalization to scale all values between 0 and 1:

$$\mathbf{H}_{\text{normalized}} = \frac{\mathbf{H} - \text{minVal}}{\text{maxVal} - \text{minVal}}$$

2.4.2 Endmember Extraction and Analysis

Image analysis using LSU (Linear Spectral Unmixing) algorithms was conducted to identify unique spectral signatures (endmembers) within the image. This aimed to discover features within the image, as endmembers can correspond to specific materials. Vertex Component Analysis (VCA), Fast Iterative Pixel Purity Index (FIPPI) and N-FINDR were chosen as endmember extraction methods and abundance maps were created to compare each method’s effectiveness.

VCA exploits the geometric property that endmembers in a hyperspectral dataset form the vertices of a simplex (Nascimento and Dias, 2005). FIPPI operates by projecting the hyperspectral data onto a high-dimensional space and identifying the pixels that are most spectrally pure (Chang and Plaza, 2006). N-FINDR operates on the principle that the purest pixels (endmembers) in a hyperspectral image will form a simplex with the maximum volume in the spectral space (Winter, 1999). VCA and N-FINDR do not require prior knowledge about the number or type of materials present, which is beneficial for brain imaging as the precise composition of the scanned area may not be known in advance. FIPPI’s method is inherently robust to noise, which is beneficial as the quality of hyperspectral images can be affected by factors such as light scattering in complex tissue.

An image analysis software, Scyven (Habili et al., 2014), provides automatic illuminant and reflectance

recovery and automatic material discovery. Scyven also implements material classification using its own LSU and preprocessing algorithms. Therefore, Scyven was used to analyse images as a reference to compare against our own developed algorithms, allowing for the assessment of VCA, N-FINDR and FIPPI as well as LSU for identifying features within brain tissue from hyperspectral images.

2.5 Imaging Mouse Brain Tissue

2.5.1 Tissue Samples

Once the above methods are validated, the HSI system can be used to image mouse brain tissue to evaluate its effectiveness when applied on the microscopic level. Samples are taken from 5xFAD mice, engineered to express abnormal accumulation of amyloid-beta (Eimer and Vassar, 2013), which is indicative of Alzheimer’s disease.

2.5.2 Obtaining and Locating Spectral Signatures

Subsequent contrasting of each pixel’s constituent end-members with already-obtained spectral signatures of the biomarker amyloid-beta (More and Vince, 2015) allows for the identification of which pixels contain amyloid-beta. The HSI system would thus give information regarding the location and abundance of Alzheimer’s biomarkers within brain tissue.

3 Results

3.1 Finger Ischaemia Test

3.1.1 The 3D Hypercube

Non-Ischaemic Finger

Figure 16 below visually illustrates the 3D hypercube dataset obtained for the normal (non-ischaemic) finger. Each column of the image target has an associated spectrogram. The dimensions of the hypercube in MATLAB are **612 x 900 x 816**. Each element in the matrix represents the intensity at a particular wavelength and spatial position. The dimensions are attributed to scaling of the 2448 x 3264p video feed by 0.25 \times , and sampling 900 frames of the video.

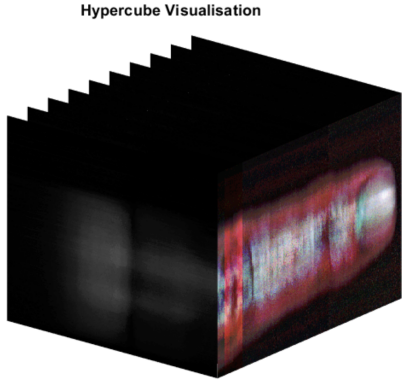


Figure 16: Hypercube Visualisation (Normal)

To examine sample spectrograms from the hypercube, the hypercube was sliced at 3 different column pixel positions and the corresponding spectrograms were displayed. Figure 17 shows that different regions of the finger have different spectral profiles.

Ischaemic Finger

The hypercube reconstruction process was repeated for the non-ischaemic finger. The results obtained can be observed in Figures 17 and 18.

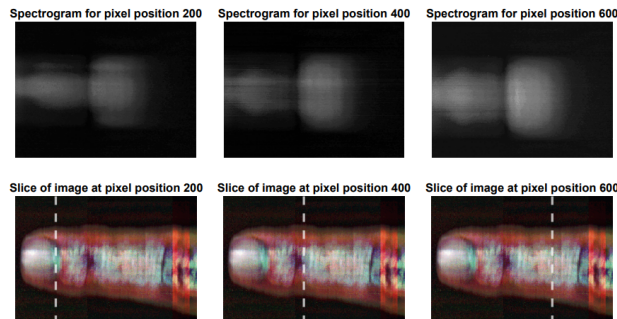


Figure 17: Spectrograms Corresponding to Different Pixels on Normal Finger

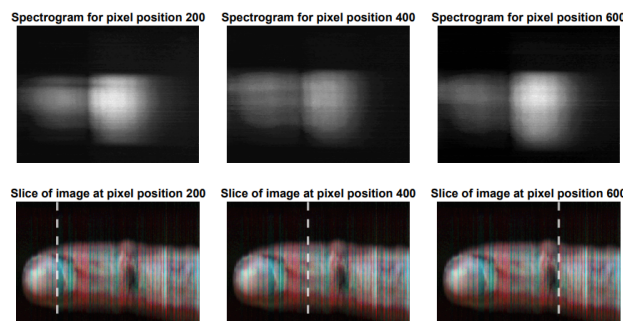


Figure 18: Spectrograms Corresponding to Different Pixels on Ischaemic Finger

3.1.2 Image Reconstruction

The images of the finger were reconstructed from the hypercube. The intensities at 3 different wavelengths, 450nm, 550nm and 650nm were extracted for the blue, green and red channels, respectively. This allowed an RGB image to be constructed as shown in Figure 19. The dimensions of the reconstructed image were 612 x 900 as expected.

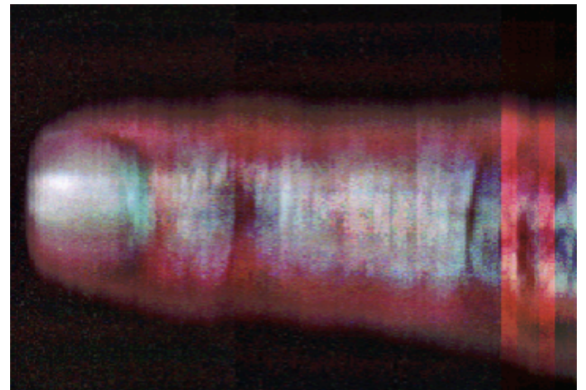


Figure 19: Reconstructed RGB Image

3.1.3 Comparing Pixel Spectra

4 points were selected at different regions of the finger. Then, their corresponding pixel spectra were plotted and compared as depicted in Figures 20 and 21.

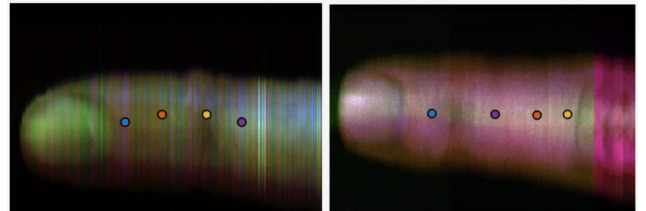


Figure 20: Four Points Selected from Each Finger

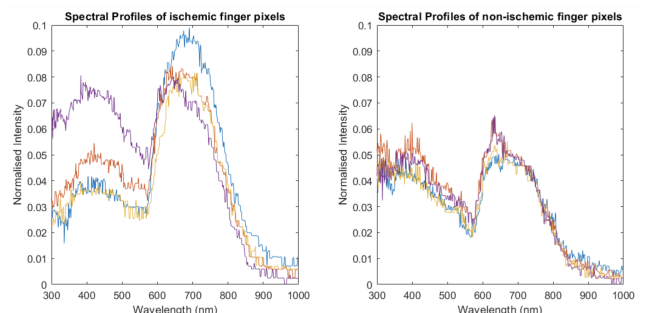


Figure 21: Spectral Profiles of Each Point

Both cases showed similar characteristics. There were peaks at around 400nm and 700nm, corresponding to

violet and red wavelength colours respectively. There was also an intensity minima at $\approx 600\text{nm}$. At higher wavelengths, intensity levels decreased exponentially with increasing wavelength.

While the spectral profiles followed a similar shape, they had different peak intensity levels. The ischaemic finger had peak intensities ranging from 0.07 to 0.09, while the non-ischaemic finger was from 0.045 to 0.065.

3.2 Proof-of-concept Image Processing

3.2.1 Preprocessing

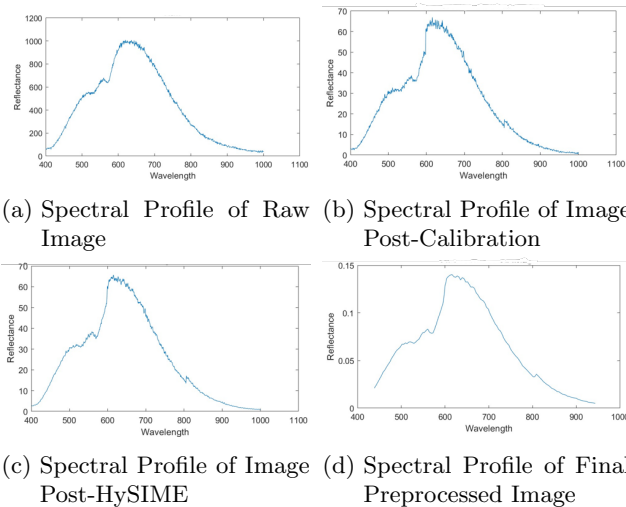


Figure 22: Preprocessing Pipeline

As seen in Figure 22, there was an increase in SNR and spectral smoothing throughout the preprocessing pipeline. However, looking at Figure 22b, the calibration process seemed to slightly increase the amount of noise in the spectral profile. After calibration, the magnitude of the reflectance shrunk to a maximum of around 67. After the HySIME algorithm in 22c, there was further increase to SNR. In the final stage of the preprocessing pipeline in 22d after the band reduction, extreme noise band removal and normalization, the spectral profile was completely smoothed with a maximum magnitude of 0.15 (due to normalization). Throughout the pipeline the overall shape of the spectral profile was retained.

3.2.2 Image Analysis

Figure 23 shows that the corruption that was irremovable in the reconstructed image carried over to end-member extraction, illustrated by the vertical lines. The three extraction methods provided different end-members: VCA (Figure 23a) and N-FINDR (Figure

23b) extracted 4 endmembers, whilst FIPPI (figure 23c) extracted 5. VCA and N-FINDR yielded very similar results, whilst FIPPI appeared the most different.

From Figure 24a, it can be seen that Scyven could reconstruct images with greater clarity and less corruption. The endmembers identified in Figure 24b were similar to those found by the VCA and N-FINDR algorithms, as shown in Figure 23.

4 Discussion

4.1 Analysis of Results

4.1.1 Pushbroom Mechanism

The pushbroom method was proven to work, having successfully reconstructed an image clearly resembling the imaged finger, as shown in Figure 25.

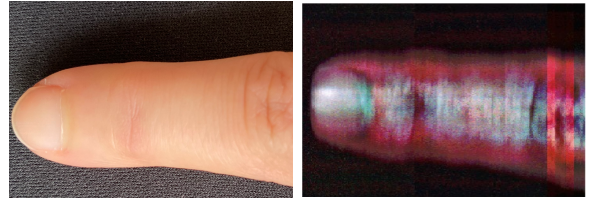


Figure 25: reconstructed image of finger using pushbroom HSI technique)

However, the makeshift set-up made it difficult to maintain a consistent quality of images. The lights illuminating the finger could not be fixed and were slightly varied in each video.

Despite the guidance markings, it was impossible to move the finger at the required rate of 0.027cm s^{-1} . Moving the finger forward too quickly resulted in gaps and artefacts in the reconstructed image, and pausing for too long may allow too much light to enter, causing sudden bursts of very bright red or green spectrums as reflected in Figure 18.

This demonstrates a trade-off between illuminating the target sufficiently and obtaining an accurate spectrogram. While our push-broom method successfully recreated the image, a more reliable way of ensuring movement at exact intervals may reduce the number of gaps and artefacts in the reconstructed image. A possible solution is moving the camera using a motorised platform at a pre-calculated speed according to the capture frame rate and target dimensions.

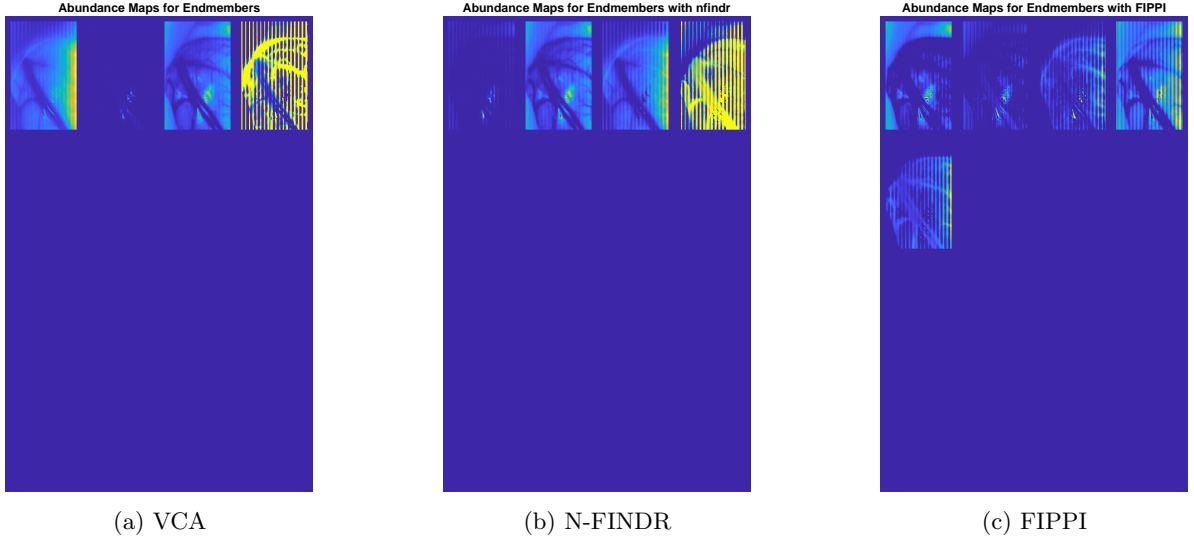


Figure 23: Abundance maps of endmembers created using different extraction methods.

4.1.2 Finger Ischaemia Validation Test

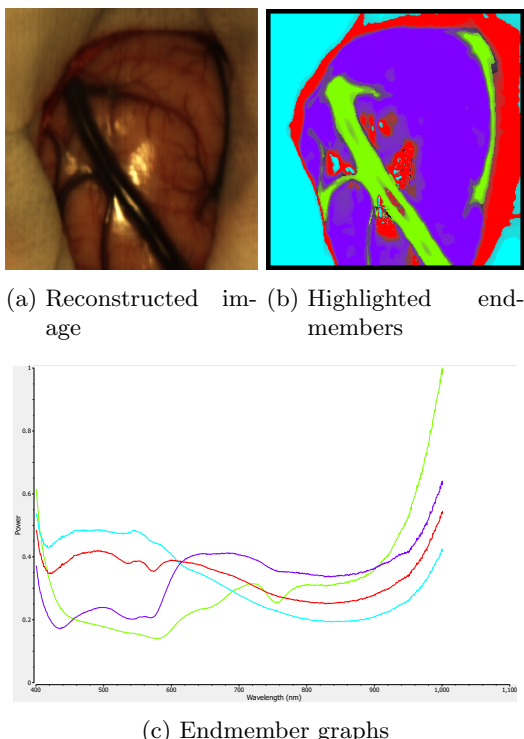


Figure 24: Image analysis using Scyven.

The finger ischaemia test was intended to validate the hyperspectral system's effectiveness at the macroscopic level.

The pushbroom method captured spectral information in a 3D hypercube. After resizing, it contained 816 spectral channels ranging from 300nm – 1000nm which is above the typical number of bands used in current HSI applications. In essence, the HSI system successfully captured high spectral information over a broad spectral range which could be further processed to obtain actionable insights.

Successfully reconstructing the images of the finger from the hypercube proved that the information obtained from the HSI system could be processed to reconstruct the target region using selected spectral bands. Nevertheless, the resolution and accuracy of the reconstructed image is dependent on the precision of the pushbroom method.

The test did not conclusively identify significant differences between ischaemic and non-ischaemic spectral profiles.

According to De Winne et al. (2024), the ischaemic finger should absorb more light and thus have lower intensity values associated across all wavelengths. This was not reflected in the pixel spectra plots. The ischaemic finger pixel spectrums had higher intensity values across wavelength values of 300nm to 800nm. This could be attributed to inconsistencies in environmental factors such as surrounding white light, or the inherent low resolution of the detector.

4.1.3 Proof-of-concept for Image Processing Pipeline

Preprocessing

Our preprocessing pipeline results in Figure 22 hold a few notable differences to those in Callico et al. (2018). The spectral curve in Figure 22b is very similar to that of the raw image which is unlike that in Figure 26. This is problematic as it indicates that the function of the calibration - to measure “the relative reflectance of any material surface independent of the spectral distribution of light and camera sensitivity” (Shaikh et al., 2021) - may not be performed. This negates the positive results achieved in the latter steps of the pipeline. Figures 22c & 22d show that the novel noise removal, dimensionality reduction and normalization algorithms used in this research are achieving their desired results. The novel HySIME algorithm performs identically to that in Callico’s paper. The novel normalization algorithm does have minor differences in the range of reflectances, likely because Callico’s approach uses a max-min algorithm on a pixel-wise basis. As the novel normalization algorithm uses the global maximum and minimum, certain pixels have reflectances that would not span the reflectance range for the entire hypercube. Whilst different, this would have minimal bearing on the pipeline’s efficacy.

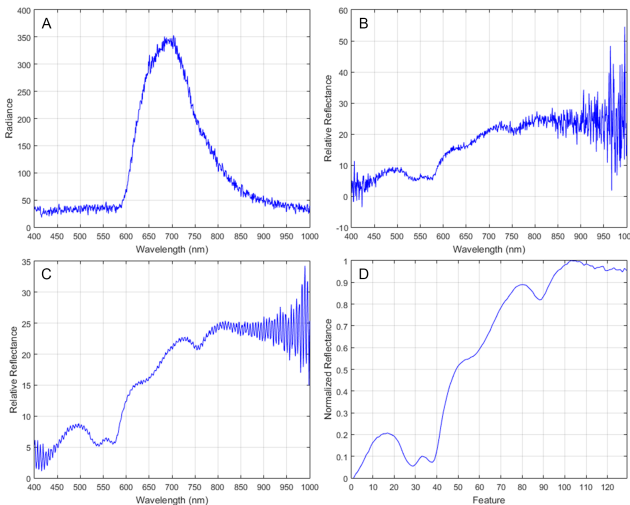


Figure 26: Preprocessing Pipeline SNR Improvement
From Callico et al.

The results to an extent validate the efficacy of the latter stages in the preprocessing pipeline for use in medical hyperspectral imaging. However, it is crucial that the radiometric calibration process is re-evaluated to understand the causation of the erroneous results before validating the proof of concept pipeline. For the intended micro-level applications, an investigation of how the principles of the pipeline would operate in this scale is needed. Assuming a multiple regression

model might be too much of a simplification, as important information that is drastically different to nearby pixels might be treated as noise and removed. For microscopic medical HSI images, more work needs to be done in testing this pipeline before any proper evaluation can be made on its efficacy.

Image Analysis

From figure 23, it is difficult to discern endmembers from any of the three extraction methods. All algorithms appeared to provide overall inaccurate results. N-FINDR appeared to be the most accurate, as it is possible to discern the different materials (veins, brain tissue etc.) from the abundance maps, as shown in Figure 23b. N-FINDR iteratively refines its choice of endmembers which likely reduced the chance of material misclassification (Plaza et al., 2004). However, the first endmember does not appear to correspond to any material.

The inaccuracies may be due to insufficient preprocessing, as corruption and noise are visible. This may also be caused by inherent flaws within the image, such as the reflected glare or shadows within the folds of the tissue. This led to endmembers which do not correspond to any distinct material or feature being identified. This issue is also present in the analysis using Scyven. As shown in Figure 24b and 24c, the endmembers labelled in red do not represent any material, and the endmembers labelled in green confused the shadows for veins.

It is clear that the innate issue with LSU is how it only takes into account the spectral information, ignoring wider context and spatial features. This means in non-perfect conditions, it classifies based on the variations in conditions rather than materials. To prevent this, our processing would have to eliminate all non-image-related variations, such as shadows and reflections, and the image must be captured with uniform lighting at an appropriate intensity. Moreover, as these algorithms are not accurate on macroscopic images of brain tissue, they are unlikely to work on microscopic images, which require increased precision to distinguish spectral features (Wu et al., 2022).

4.2 Limitations

4.2.1 Hardware limitations

Hardware components

Maintaining the cleanliness of delicate optical components like the diffraction grating and lenses using lens tissue, tweezers, and lens cleaning blower was a high priority. This was difficult given that the device had

to be deconstructed and reassembled multiple times. As a result, minor infractions in the spectrograms obtained are likely due to dust or misalignments about the optical centre of the device. Delivery times associated with replacing parts would also delay the timeline of the project significantly.

Unlike existing literature, the detector was not sensitive enough to produce a visible spectrogram under ambient light even after increasing the exposure time with AMCap. An external white light source was needed, which led to inconsistent lighting across the images, potentially affecting the results.

Image acquisition

A rudimentary pushbroom imaging mechanism was tested which involved marking regular intervals on the table surface and moving the finger at a calculated pace. This resulted in vertical artefacts due to variations in the finger movement speed. Moreover, the innate human error in this setup may also cause the dimensions of the finger in the reconstructed image to be innaccurate.

4.2.2 Software limitations

The image processing algorithms were computationally expensive and took a significant amount of time to run on personal computers. This reduced the efficiency of troubleshooting and hinders their use in real time analysis. More powerful computers may enable the discovery of a more appropriate processing pipeline for potential field use.

5 Conclusion

5.1 Summary

The following aims were set at the beginning of the project:

1. To build an inexpensive HSI system using accessible parts.
2. To calibrate and validate the HSI system for macro-imaging using the pushbroom technique, using a finger ischaemia test.
3. To integrate the imager into a microscope and image mouse brain tissue samples to prove that a low-cost HSI system can be used for micro medical applications.

The first two aims were achieved. A HSI camera was

assembled using off-the-shelf parts, and then calibrated and tested. The reconstructed image from the spectrograms obtained closely resembled the object imaged, validating the pushbroom technique. The finger ischaemia test could not reach the theoretically correct conclusion identifying the difference between the ischaemic and non-ischaemic fingers. A higher resolution camera and a more robust pushbroom mechanism would help us obtain more precise data to detect the physiological changes in tissue oxygen levels.

The system has yet to be validated for micro applications, as specified in the third aim. Whilst elements of the preprocessing pipeline can be said to validate its usage as a macro HSI preprocessing algorithm, more advanced algorithms are still required for use on micro medical applications, such as identifying fine differences in brain tissue features.

5.2 Future Work

Moving forward, the validation of the HSI system will be extended via the imaging of Alzheimer's diseased and healthy mice brain tissue samples. The HSI camera will replace the microscope camera such that the magnified sample is within the imager's FOV. Applying the pushbroom technique to the microscope stage, slices of the tissue will be imaged. As an additional improvement, the pushbroom mechanism could be automated for more precision. Furthermore, a new monochromatic detector with increased spectral resolution will be used.

Once more accurate data hypercubes have been acquired, the proof of concept algorithms will be applied to both the finger and the microscopic images. An alternate spatial classification method alongside LSU will be developed, such as using Generative Adversarial Networks or Support Vector Machines classification.

6 Appendix

6.1 Bill of Materials

Refer to Table 2.

6.2 Project Management

Describe in no more than 200 words departures from project planning (as laid out in the Project Pitch)

The Gantt chart shown in Figure 27 details our project plan as laid out in the project pitch. While the steps of the plan were followed, the parts took longer than expected to deliver, especially our detector. Thus, the assembly of the camera and all subsequent steps were delayed. We obtained all the initial parts required at the start of February but encountered issues with the diffraction grating, which we had to replace along with the housing.

Furthermore, the acquisition of a spectrogram and therefore calibration of the camera took longer than expected. We faced challenges in aligning the slit perfectly, as well as with maintaining enough brightness for an object to be imaged clearly under ambient lighting conditions. We were finally able to increase the exposure of the camera using AMCap, and obtained spectra bright enough to be analysed. The processing of database images was still done in parallel to these building and acquisition steps, and the finger ischaemia test was done before April. However, the imaging of mouse brain samples in the lab had to be delayed until May.



Figure 27: Project Pitch Gantt Chart

Provide 3 key project management lessons, each not exceeding 150 words

Firstly, through this project, we learned the importance of contingency planning. While familiar with risk management and project limitations, the risks associated with this project were underestimated. This

was especially prominent since this project involved many specific optical components, meaning there was a scarce supply of these components and high risk of them needing to be replaced. Preparing multiple backup components from different or more reliable suppliers would have saved significant time in terms of getting the system assembled, calibrated, and ready to use. Although this may lead to increased expenses, this can be mitigated through additional due diligence.

Secondly, more comprehensive research on the components of our device throughout this project would have saved time and reduced expenses. For example, the detector may have been inexpensive but lacked the resolution required and stored data in the YUV format as opposed to monochromatic intensity values, leading to a replacement detector being required. Additionally, because we were unfamiliar with lens mounts, time was wasted as we struggled to align the components precisely about the optical centre. Furthermore, we initially encountered difficulties using MATLAB to view spectrograms, as we could not control the camera's frame rate. Thus, we had to contact the manufacturers of the detector to find an appropriate application that could increase the camera exposure and rectify this issue. This highlighted the importance of actively seeking and researching solutions upon encountering challenges with our components.

Finally, we learnt to organise all meeting notes and materials in a more topical manner as opposed to in chronological order. During the project, we kept a OneNote folder containing all our project material separated into meeting minutes, literature, presentation content, and report drafts. For our meeting minutes, we created a new document each week labelled with the meeting date, and recorded all notes chronologically. This arrangement was logical and easy to implement. However, it quickly became difficult for us to locate specific information from the extensive number of meeting pages, as it was difficult to recall what content was covered in each meeting. Hence, a better approach would have been to populate each meeting's minutes with an agenda and a to-do list, and subsequently sort the discussed content into pages organised by topic. This approach was successfully employed towards the latter stages of our project.

6.3 Code Repository

Below is the link to the repository that contains the code used throughout the project. It includes the scripts used for constructing the hypercube, processing and analysing the data, as well as creating plots used in the report.

<https://github.com/racketmaestro/Hyperspectral-Imaging>

Table 2: Final HSI System Components

#	Part #	Item	Supplier	Quantity	Total Cost/£
1	83-107	16.0mm FL, No IR-Cut Filter, f/4, Micro Video Lens	Edmund Optics	1	47.60
2	64-102	M12 Lock Nut	Edmund Optics	1	11.90
3	S20HK	$\varnothing 1/2"$ Mounted Slit, 20 \pm 2 μ m Wide, 3 mm Long	Thorlabs	1	94.20
4	63-519	10.0mm Dia. X 10.0mm FL, VIS-NIR Coated, Plano-Convex Lens	Edmund Optics	1	33.15
5	63-943	10mm Diameter, S-Mount Thin Optic Mount	Edmund Optics	3	85.41
6	63-953	17.5mm - 25mm Length, S-Mount Fine Focus Tube	Edmund Optics	1	50.83
7	63-523	10.0mm Dia. X 30.0mm FL, VIS-NIR Coated, Plano-Convex Lens	Edmund Optics	1	32.73
8	49-580	600 Grooves, 25mm Sq, 28.7° Groove Angle Grating	Edmund Optics	1	99.45
9	56-776	25.0mm FL, No IR-Cut Filter, f/2.5, Micro Video Lens	Edmund Optics	1	56.95
10	-	Spinel 8MP USB Camera Module Sony IMX179 Sensor	Spinel	1	122.40
Total:					634.62
11	53-675	C-Mount to M12 Lens Adapter	Edmund Optics	1	23.80
12	GT13-06V	Visible Transmission Grating, 600 Grooves/mm, 28.7° Groove Angle	Thorlabs	1	72.70
13	24-162	IDS Imaging U3-3841XLE-M-GL 1/3" Monochrome Board Level USB3 Camera	Edmund Optics (formerly)	1	No longer known

References

- Akbari, H., Kosugi, Y., Kojima, K., and Tanaka, N. (2008). Hyperspectral imaging and diagnosis of intestinal ischemia. *Annual International Conference of the IEEE Engineering in Medicine and Biology Society. IEEE Engineering in Medicine and Biology Society. Annual International Conference*, 2008:1238–1241.
- Caballero, D., Calvini, R., and Amigo, J. M. (2020). Hyperspectral imaging in crop fields: precision agriculture. *Data Handling in Science and Technology*, 32:453–473.
- Callico, G. M., Jo, J. A., Farinella, G. M., Kiran, B. R., Sosa, C., Bulters, D., Bulstrode, H., Szolna, A., Piñeiro, J. L., Kabwama, S., Madronal, D., Lazcano, R., J-O'Shanahan, A., Bisshopp, S., Hernandez, M. H., Baez, A., Yang, G.-Z., Stanciulescu, B., Salvador, R., Juarez, E., and Sarmiento, R. (2018). Spatio-spectral classification of hyperspectral images for brain cancer detection during surgical operations. *PLOS ONE*, 13:e0193721–e0193721.
- Cao, F., Yang, Z., Ren, J., Jiang, M., and Ling, W.-K. (2017). Does normalization methods play a role for hyperspectral image classification?
- Chang, C.-I. and Plaza, A. (2006). A fast iterative algorithm for implementation of pixel purity index. *IEEE Geoscience and Remote Sensing Letters*, 3:63–67.
- De Winne, J., Strumane, A., Babin, D., Luthman, S., Luong, H., and Philips, W. (2024). Multispectral indices for real-time and non-invasive tissue ischemia monitoring using snapshot cameras. *Biomedical Optics Express*, 15:641–655.

- Dell'Endice, F., Nieke, J., Koetz, B., Schaepman, M. E., and Itten, K. (2009). Improving radiometry of imaging spectrometers by using programmable spectral regions of interest. *ISPRS Journal of Photogrammetry and Remote Sensing*, 64:632–639.
- Edmund Optics, A. (2024). Hyperspectral and multispectral imaging — edmund optics.
- Eimer, W. A. and Vassar, R. (2013). Neuron loss in the 5xfad mouse model of alzheimer's disease correlates with intraneuronal ab42 accumulation and caspase-3 activation. *Molecular Neurodegeneration*, 8:2.
- Fabelo, H., Ortega, S., Szolna, A., Bulters, D., Piñeiro, J. F., Kabwama, S., J-O'Shanahan, A., Bulstrode, H., Bisshopp, S., Kiran, B. R., Ravi, D., Lazcano, R., Madroñal, D., Sosa, C., Espino, C., Marquez, M., De La Luz Plaza, M., Camacho, R., Carrera, D., Hernández, M., Callicó, G. M., Morera Molina, J., Stanciulescu, B., Yang, G.-Z., Salvador, R., Juárez, E., Sanz, C., and Sarmiento, R. (2019). In-vivo hyperspectral human brain image database for brain cancer detection. *IEEE Access*, 7:39098–39116.
- Feng, X., He, L., Cheng, Q., Long, X., and Yuan, Y. (2020). Hyperspectral and multispectral remote sensing image fusion based on endmember spatial information. *Remote Sensing*, 12:1009.
- Feng, Y.-Z. and Sun, D.-W. (2012). Application of hyperspectral imaging in food safety inspection and control: A review. *Critical Reviews in Food Science and Nutrition*, 52:1039–1058.
- Habili, N., Oorloff, J., and Wei, R. (2014). Scyven – scyllarus – hyperspectral image processing.
- Hadoux, X., Hui, F., Lim, J. K. H., Masters, C. L., Pébay, A., Chevalier, S., Ha, J., Loi, S., Fowler, C. J., Rowe, C., Villemagne, V. L., Taylor, E. N., Fluke, C., Soucy, J.-P., Lesage, F., Sylvestre, J.-P., Rosa-Neto, P., Mathotaarachchi, S., Gauthier, S., Nasreddine, Z. S., Arbour, J. D., Rhéaume, M.-A., Beaulieu, S., Dirani, M., Nguyen, C. T. O., Bui, B. V., Williamson, R., Crowston, J. G., and van Wijngaarden, P. (2019). Non-invasive in vivo hyperspectral imaging of the retina for potential biomarker use in alzheimer's disease. *Nature Communications*, 10.
- Heo, C. (2019). Construction of a hyperspectral camera using off-the-shelf parts and 3d-printed parts. *Mechanical Engineering Undergraduate Honors Theses*.
- Hollows, G. and James, N. (2024). Understanding focal length and field of view — edmund optics.
- Lu, G. and Fei, B. (2014). Medical hyperspectral imaging: a review. *Journal of Biomedical Optics*, 19:010901.
- Mao, Y., Betters, C. H., Evans, B., Artlett, C. P., Leon-Saval, S. G., Garske, S., Cairns, I. H., Cocks, T., Winter, R., and Dell, T. (2022). Openhsi: A complete open-source hyperspectral imaging solution for everyone. *Remote Sensing*, 14:2244–2244.
- More, S. S. and Vince, R. (2015). Hyperspectral imaging signatures detect amyloidopathy in alzheimer's mouse retina well before onset of cognitive decline. *ACS Chemical Neuroscience*, 6:306–315.
- Morris, R. (2021). Collimating lenses - their importance in spectroscopy.
- Nascimento, J. and Bioucas-Dias, J. (2007). Hyperspectral signal subspace estimation. *CiteSeer X (The Pennsylvania State University)*.
- Nascimento, J. and Dias, J. (2005). Vertex component analysis: a fast algorithm to unmix hyperspectral data. *IEEE Transactions on Geoscience and Remote Sensing*, 43:898–910.
- Plaza, A., Martinez, P., Perez, R., and Plaza, J. (2004). A quantitative and comparative analysis of endmember extraction algorithms from hyperspectral data. *IEEE Transactions on Geoscience and Remote Sensing*, 42(3):650–663.
- Riedl, M. J. (2001). *Optical Design Fundamentals for Infrared Systems, Second Edition*, volume TT48. SPIE, 2 edition.
- Salazar-Vazquez, J. and Mendez-Vazquez, A. (2020). A plug-and-play hyperspectral imaging sensor using low-cost equipment. *HardwareX*, 7:e00087.
- Shaikh, M. S., Jaferzadeh, K., Thornberg, B., and Caselgren, J. (2021). Calibration of a hyper-spectral imaging system using a low-cost reference. *Sensors*, 21:3738.
- Shaw, G. and Burke, H.-H. (2003). Spectral imaging for remote sensing spectral imaging for remote sensing. *LINCOLN LABORATORY JOURNAL*, 14.
- Shimoni, M., Haelterman, R., and Perneel, C. (2019). Hyperpectral imaging for military and security applications: Combining myriad processing and sensing techniques. *IEEE Geoscience and Remote Sensing Magazine*, 7:101–117.
- Sigernes, F., Syrjäsuo, M., Storvold, R., Fortuna, J., Grøtte, M. E., and Johansen, T. A. (2018). Do it yourself hyperspectral imager for handheld to airborne operations. *Optics Express*, 26:6021.
- Stuart, M. B., Stanger, L. R., Hobbs, M. J., Pering,

T. D., Thio, D., McGonigle, A., and Willmott, J. R. (2020). Low-cost hyperspectral imaging system: Design and testing for laboratory-based environmental applications. *Sensors (Basel)*, 20:3293–3293.

Therien, C. (2018). Pysptools documentation — pysptools 0.15.0 documentation.

van der Meer, F. D., van der Werff, H. M., van Ruitenbeek, F. J., Hecker, C. A., Bakker, W. H., Noomen, M. F., van der Meijde, M., Carranza, E. J. M., Smeth, J. B. d., and Woldai, T. (2012). Multi- and hyperspectral geologic remote sensing: A review. *International Journal of Applied Earth Observation and Geoinformation*, 14:112–128.

Wang, Y., Fu, X., Chen, Y., Q, L., Ning, Y., and Wang, L. (2022). The development progress of surface structure diffraction gratings: From manufacturing technology to spectroscopic applications. *Applied sciences*, 12:6503–6503.

Winter, M. (1999). N-findr: an algorithm for fast autonomous spectral end-member determination in hyperspectral data. *Proc. SPIE 3753, Imaging Spectrometry V*.

Wu, Y., Xu, Z., Yang, W., Ning, Z., and Dong, H. (2022). Review on the application of hyperspectral imaging technology of the exposed cortex in cerebral surgery. *Frontiers in Bioengineering and Biotechnology*, 10.

Yoon, J. (2022). Hyperspectral imaging for clinical applications. *BioChip Journal*, 16:1–12.

Yuen, P. W. and Richardson, M. (2010). An introduction to hyperspectral imaging and its application for security, surveillance and target acquisition. *The Imaging Science Journal*, 58:241–253.